1.5.5.4.2 Crystalline electric fields

The magnetic properties of Heusler alloys containing rare earth elements are characterised by the crystal field environment. The basic crystal field splitting depends only on J and the point symmetry of the rare earth ion. However, quantitative details will depend upon the radial extent of the wave function. In practice, relativistic band structure calculations are usually not available, so the quantities which depend upon the radial extent of the wave function are adjusted to fit the experimental observation. In the $L2_1$ structure the rare-earth atoms occupy the octahedral site which has point symmetry (m3m). The single-ion Hamiltonian may then be written as:

$$H_{CEF} = B_4^0 \cdot \left(0_4^0 + 5 \cdot 0_4^4\right) + B_6^0 \cdot \left(0_6^0 - 21 \cdot 0_6^4\right) \tag{59}$$

where B_4^0 and B_6^0 are C.F. parameters which measure the strength of the fourth and sixth order terms of the electric potential and 0_n^m are Stevens operators [52S1]. Following Lea et al [62L1] the C.F. parameters may be parameterised as $B_4F_4 = Wx, B_6F_6 = W(1-|x|)$ with F_4 and F_6 being numerical factors. The W parameter determines the overall splitting and x measures the overall strength of the fourth to sixth order terms with $-1 \le x \le 1$. Thus eq. (59) becomes

$$H_{CEF} = W \cdot \left\{ \frac{x}{F_4}\left(0_4^0 + 5 \cdot 0_4^4\right) + \frac{1-|x|}{F_6}\left(0_6^0 - 21 \cdot 0_4^0\right) \right\} \tag{60}$$

For a given W and x, the relative energy as well as the eigenfunctions for each state can be found by diagonalising the Hamiltonian.

The most direct method of investigating C.F. parameters is by inelastic neutron scattering experiments. Neutron scattering probes not only the eigenvalues but also the eigenfunctions through transition intensities.

The cross-section for the scattering of unpolarised neutrons from the initial state $|i\rangle$ to the final state $|f\rangle$ that belongs to a single J multiplet of a system of N non-interacting magnetic ions is given by:

$$\frac{d^2\sigma}{d\Omega dE} = N\left[\frac{1.91e^2}{2m_nc^2}\right]^2 g_J^2 f^2(Q) \frac{k_f}{k_i} \sum_{i,f} P_i \left|\left\langle f \left| \bar{J}_\perp \right| i \right\rangle\right|^2 \delta(E_i - E_f - E) \tag{61}$$

The energies $E_{i,f}$ of the crystal-field levels are independent of the momentum transfer $\hbar Q$, while the intensity of the scattering generally decreases monotonically with increasing Q through the magnetic form factor $f^2(Q)$. The thermal dependence of the scattering enters via the occupational probabilities P_i, which for non-interacting systems is described by Boltzmann statistics, since the ions are distinguishable by their lattice positions. The relative scattering intensity between two transitions is simply the ratio of $\sum_{if} P_i \left|\left\langle f \left| \bar{J}_\perp \right| i \right\rangle\right|^2$ for the two transitions. The matrix elements obtained by diagonalising the Hamiltonian for a given x have been tabulated by Birgeneau as a function of x for various J multiplets.

Within an isostructural series of rare earth alloys, it is often a good approximation to assume that the electronic band structure and electron distribution within the unit cell is not appreciably changed when one rare earth element is replaced by another one. This assumption naturally leads to a scaling of C.F. parameters for the various rare earth compounds within an isostructural series according to

$$A_n a^{n+1} = \frac{B_n a^{n+1}}{\Theta_n < r^n >} \tag{62}$$

where Θ are reduced matrix elements [62L1], $<r^n>$ the expectation values of powers of the radial part of the f-electron wave function [79F1] and a^{n+1} is the (n+1)th power of the lattice parameter.

Recently it has been found that such scaling also works reasonably well for Pd_2RZ for which the rare earth element R is kept fixed and Z is changed from In to Sn. The level scheme is experimentally found to not change significantly between these alloys. However, there is an overall change in the energy scale of the crystal field level scheme. In the Heusler structure the rare earth element sits in the centre of a cube with eight Pd atoms as nearest neighbours. Thus, the Pd atoms are responsible for the crystal field splitting of the 4f electron wave functions on the rare earth atom. Since In or Sn are at the centre of adjacent Pd cubes they have little direct influence on the magnitude of matrix elements determining the C.F. splitting. Changing In by Sn alters the conduction electrons at the expense of increasing the charge on the ion at the In/Sn site. The increase of this point charge has negligible direct influence on the C.F. splitting. However, the additional conduction electrons are more delocalised and partly screen the charge on the Pd atoms. Consequently the overall splitting is expected to be reduced on going from In to Sn, whilst the level sequence is maintained. This has been observed experimentally in the $Pd_2Ho(In, Sn)$ and $Pd_2Er(In, Sn)$ systems [95B1].

X_2YZ X = 3d, Y = 4f

X = 1B: Cu
Y = 4A: Ce
Z = 3B: In

Cu_2CeIn

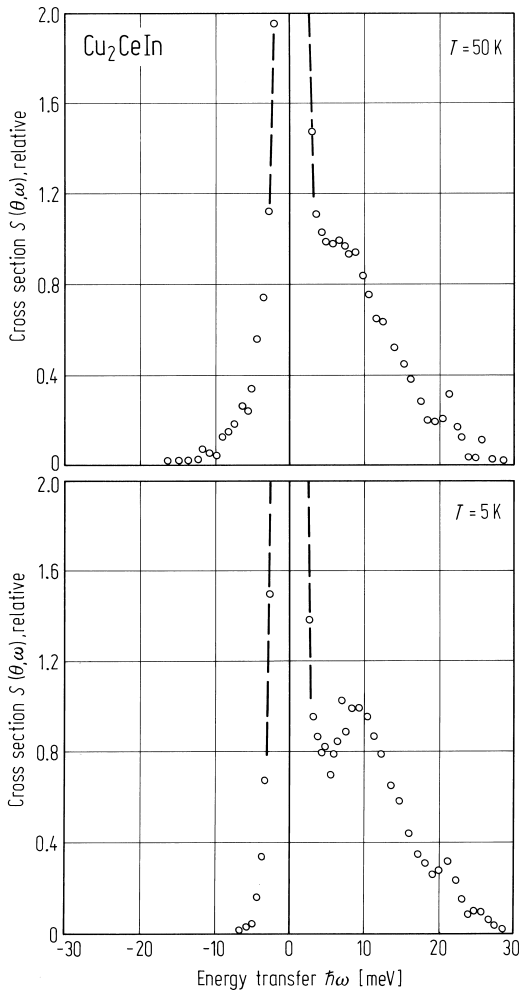

Fig. 222. Neutron cross-section for Cu_2CeIn as a function of temperature [87L1].

X = 8A: Pd; 1B: Ag
Y = 4A: Ce, Pr, Nd, Ho, Er, Yb
Z = 3B: In; 4B: Sn

Pd_2YSn

Table 50. CEF parameters, CEF level sequences, overall energy splitting and ground state status for various trivalent rare-earth ions in RPd_2Sn compounds. OES: overall energy splitting in meV. GSS: ground state (M: magnetic, NM: non-magnetic) [89L1].

R	W [meV]	x	OES	GSS	CEF engery level sequence
Tb [a])	0.053	– 0.785	10.71	M/NM [b])	$\Gamma_3/\Gamma_5^{(1)} - \Gamma_5^{(2)} - \Gamma_2 - \Gamma_4 - \Gamma_1$
Dy [a])	– 0.036	– 0.509	11.80	M	$\Gamma_8^{(3)} - \Gamma_8^{(2)} - \Gamma_7 - \Gamma_8^{(1)} - \Gamma_6$
Ho [c])	0.0287	0.3248	17.56	M	$\Gamma_5^{(1)} - \Gamma_3^{(1)} - \Gamma_4^{(1)} - \Gamma_5^{(2)} - \Gamma_1 - \Gamma_4^{(2)} - \Gamma_3^{(2)}$
Er [c])	– 0.0450	0.3022	20.32	M	$\Gamma_8^{(3)} - \Gamma_6 - \Gamma_8^{(2)} - \Gamma_8^{(1)} - \Gamma_7$
Er [a])	– 0.040	0.292	18.23	M	$\Gamma_8^{(3)} - \Gamma_6 - \Gamma_8^{(2)} - \Gamma_8^{(1)} - \Gamma_7$
Tm [a])	0.076	– 0.513	11.98	M/NM [b])	$\Gamma_5^{(1)}/\Gamma_3 - \Gamma_5^{(2)} - \Gamma_2 - \Gamma_4 - \Gamma_1$
Yb [a])	– 0.530	– 0.722	13.43	M	$\Gamma_7 - \Gamma_8 - \Gamma_6$

[a]) Scaled parameters.
[b]) Scaled x is in the region of LLW diagram where Γ_3 and $\Gamma_5^{(1)}$ are crossing. The ground is therefore uncertain.
[c]) Experimentally determined.

Table 51. CEF field parameters B_4^0 and B_6^0 and values of $|J_{sf}|$ obtained from the suppression of T_C data on $Pd_2Y_{1-x}R_xSn$ assuming $N(0) = 0.3$ states/eV-atom spin direction (a) for a free rare-earth ion; (b) with CEF effects; (c) with CEF and assuming T_C to scale with the lattice parameters between Pd_2YSn and Pd_2LuSn. The error in $|J_{sf}|$ based on the experimental results is ± 20 % [85U3].

Rare-earth impurity	B_4^0 [10^{-2} K]	B_6^0 [10^{-4} K]	$\|J_{sf}\|$ [eV]		
			(a)	(b)	(c)
Gd			0.025	0.025	0.025
Dy	– 0.61	0.38	0.020	0.028	0.028
Ho	0.32	0.41	0.016	0.020	0.020
Er	– 0.39	– 0.60	0.020	0.023	0.023
Tm	– 0.014	1.48	0.020	0.026	0.019
Yb	0.13	– 33.0	0.039	0.047	0.033

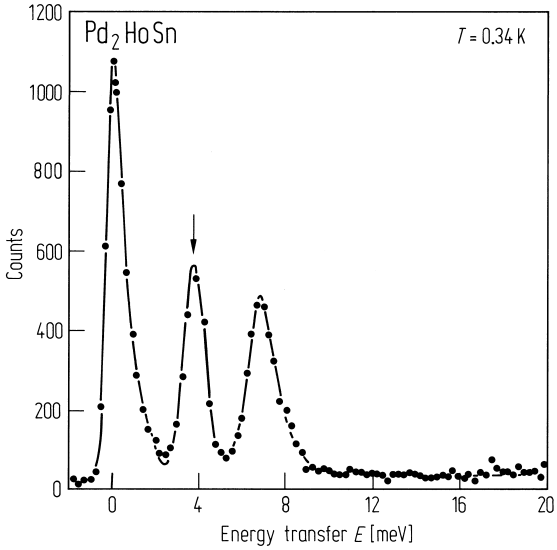

Fig. 223. Elastic and inelastic scattering at a wavevector Q = 1.8 Å^{-1} observed at 0.34 K (in the magnetic state) on a powder sample of Pd_2HoSn using the triple-axis technique. The transitions at 3.5 and 6.7 meV are crystal-field excitations. Additional intensity on the shoulder of the peak at 6.7 meV is another crystal-field excitation at 7.5 meV. The scattering at low energies does not have the correct temperature or wavevector dependence to be interpreted as crystal field in origin [89L1]. E_i = 14.8 meV.

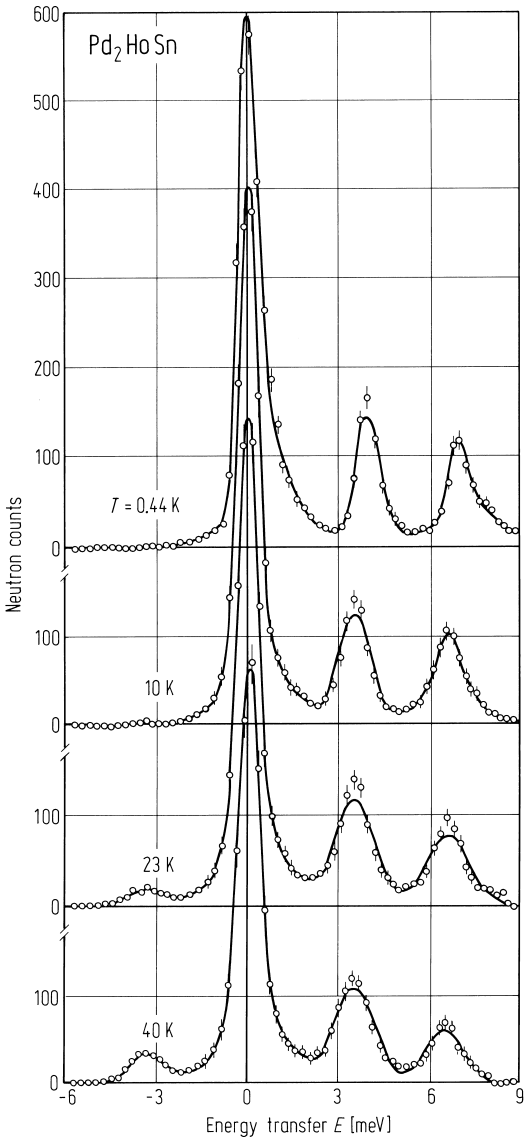

Fig. 224. Elastic and inelastic scattering observed on powder Pd_2HoSn with the time-of-flight technique. To improve the statistics, spectra shown were obtained by summing over data acquired on 60 detectors spanning a $\boldsymbol{Q}$ range from 0.48 to 3.85 Å^{-1}. At T = 23 and 40 K, transitions from higher-energy levels to lower-energy levels are also evident in neutron energy gain (E < 0) [89L1]. E_i = 13.8 meV.

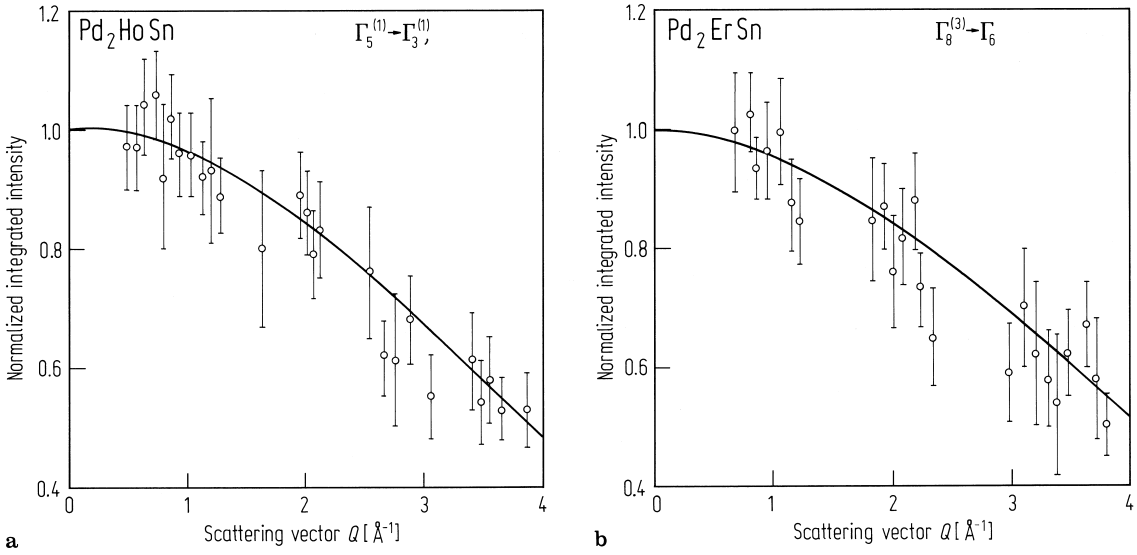

Fig. 225. ***Q*** dependence of the intensities of the excitations for (**a**) Pd_2HoSn at 3.52 meV, and for (**b**) $ErPd_2Sn$ at 7.43 meV and 10.0 K. The solid circles are the intensities observed in different detectors, and the data have been normalised to unity at small *Q*. The solid curves are theoretical calculations for the square of magnetic form factors for the appropriate rare earth ion, Ho^{3+} and Er^{3+}, respectively [89L1].

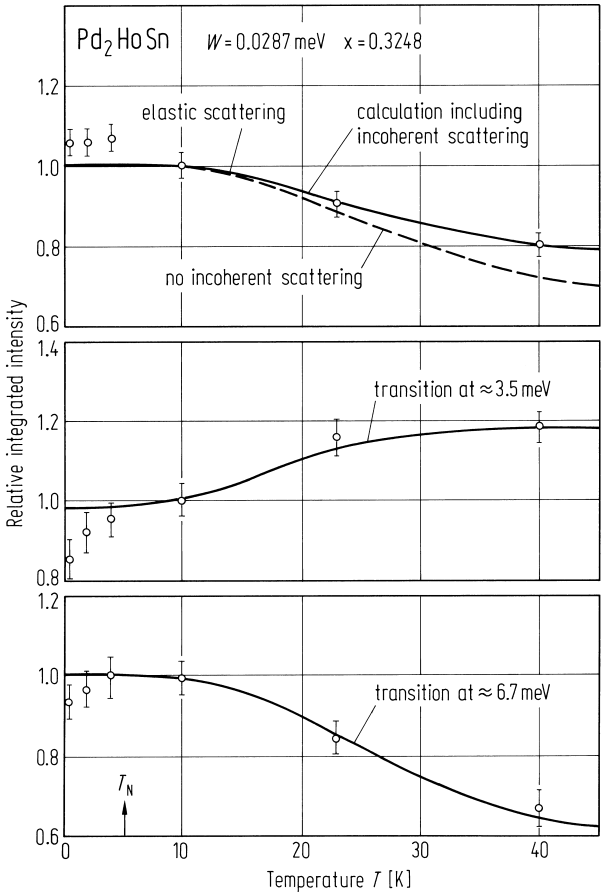

Fig. 227. Comparison of the temperature dependence of the intensity of the calculated (solid curves) and observed (circles) elastic scattering, as well as the crystal-field transitions, for Pd_2HoSn. Well above the Néel temperature the non-interacting single-ion model provides a good fit to the observations. Below T_N on the other hand, there are systematic deviations from the single-ion model, as might be expected [89L1].

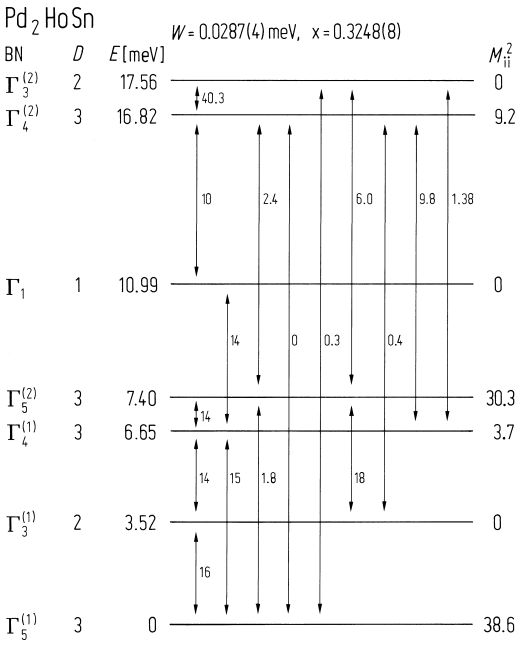

Fig. 226. CEF level scheme for Ho^{3+} in cubic Pd_2HoSn. The arrows indicate possible inelastic transitions, and the corresponding numbers give the value for the dipole transition probability matrix elements $\left|\langle i|J_z|j\rangle\right|^2$. BN ≡ Bethe's notation, D ≡ Degeneracy and the diagonal elements M_{ii} give the elastic scattering probability [89L1].

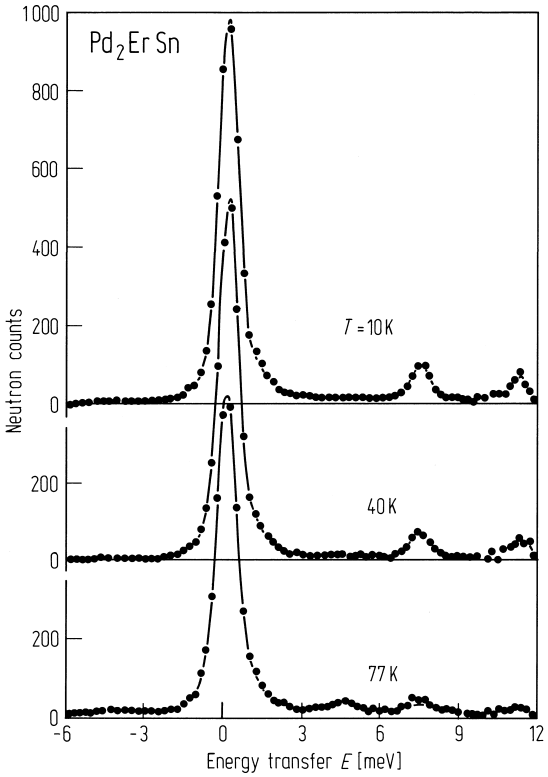

Fig. 228. Spectra of crystal field excitations for Pd_2ErSn obtained by time-of-flight techniques. At T = 77.0 K, crystal-field transitions between excited states are also evident at – 4.25 and 4.25 meV [89L1]. E_i = 14.8 meV.

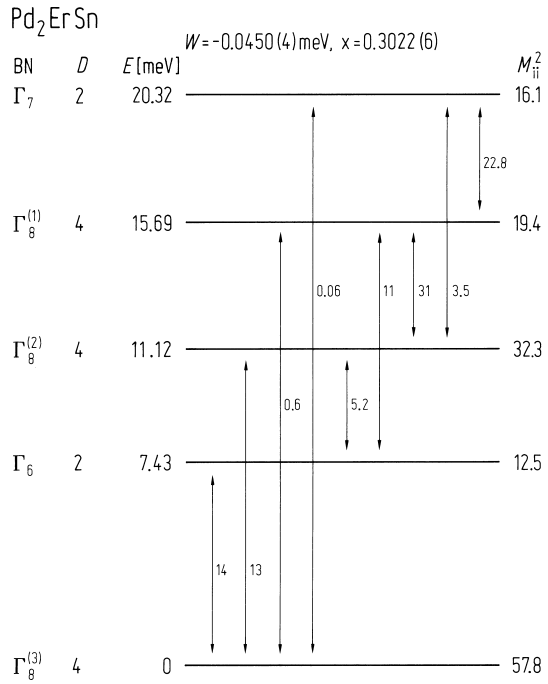

Fig. 229. CEF level scheme for Er^{3+} in cubic Pd_2ErSn. The notation is the same as that for Fig. 226 [89L1].

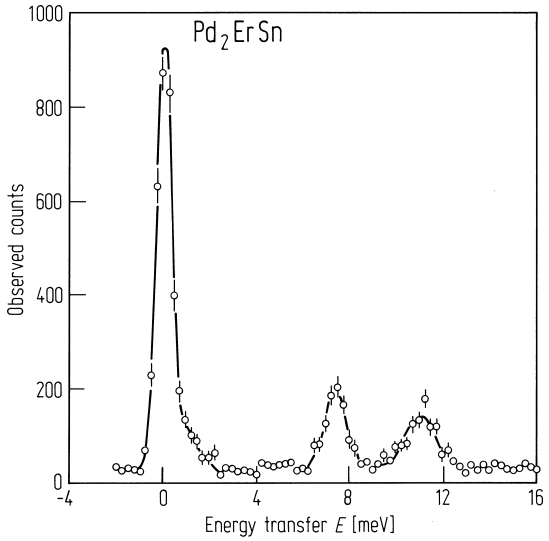

Fig. 230. Inelastic neutron scattering observed at 0.8 K, i.e. below the Néel temperature of Pd_2ErSn. The transitions at 7.4 and 11.1 meV are crystal field excitations. There was no change in the excitation energies or intensities on changing to 3 K, i.e. into the paramagnetic state [87S4].

Pd_2YIn

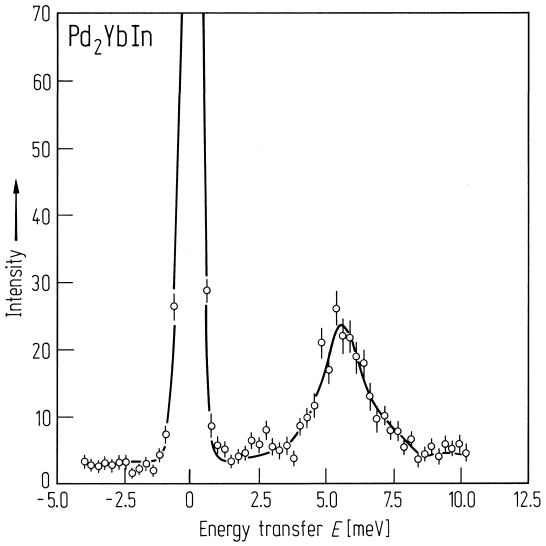

Fig. 231. Inelastic neutron spectrum of Pd_2YbIn for T = 10 K at constant scattering vector Q = 2.0 Å^{-1}. The full line is a guide to the eye [95B2].

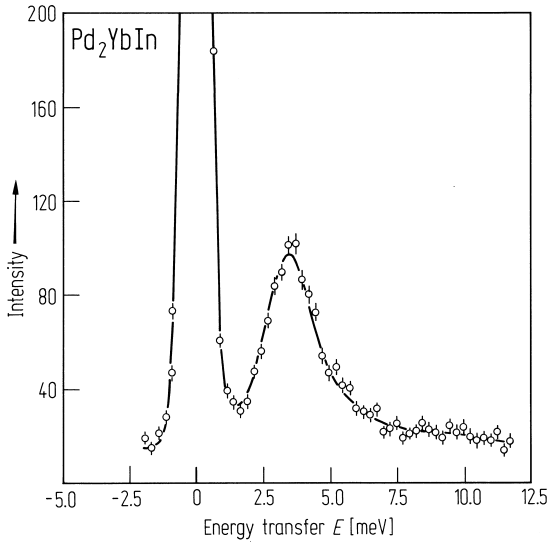

Fig. 232. Experimental inelastic neutron scattering spectrum of Pd_2YbIn at T = 10 K and a scattering vector of Q = 3.5 Å^{-1} [95B2].

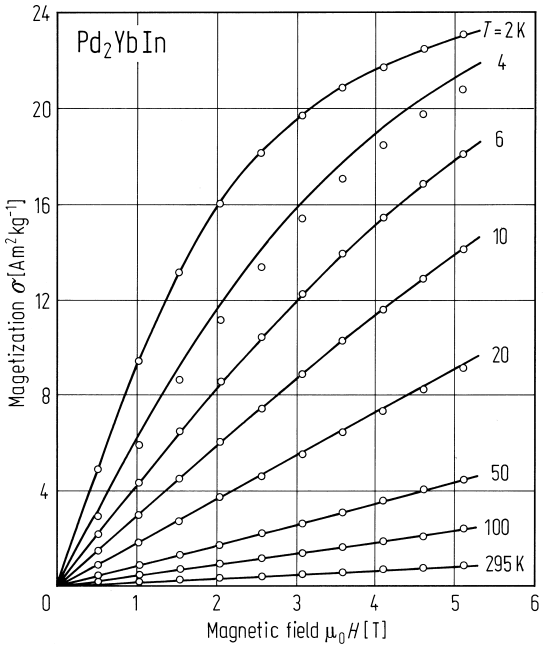

Fig. 233. Experimental magnetisation data (circles) of Pd_2YbIn. The lines are a fit of a crystal electric field model to the data [95B2].

Ag_2YIn

Table 52. Crystal field parameters and ground states of three compounds in the Ag_2(R)In series [84G1].

Compounds	Ground state	W [K]	x	$A_4\langle r^4\rangle$ [K]	$A_6\langle r^6\rangle$ [K]
$CeInAg_2$	Γ_7	2.9 ± 0.5	1	7.6	
$PrInAg_2$	Γ_3	-1.2 ± 0.2	0 ± 0.02	0	-14.9
$NdInAg_2$	Γ_6	1.2 ± 0.2	0 ± 0.02	0	-12.6

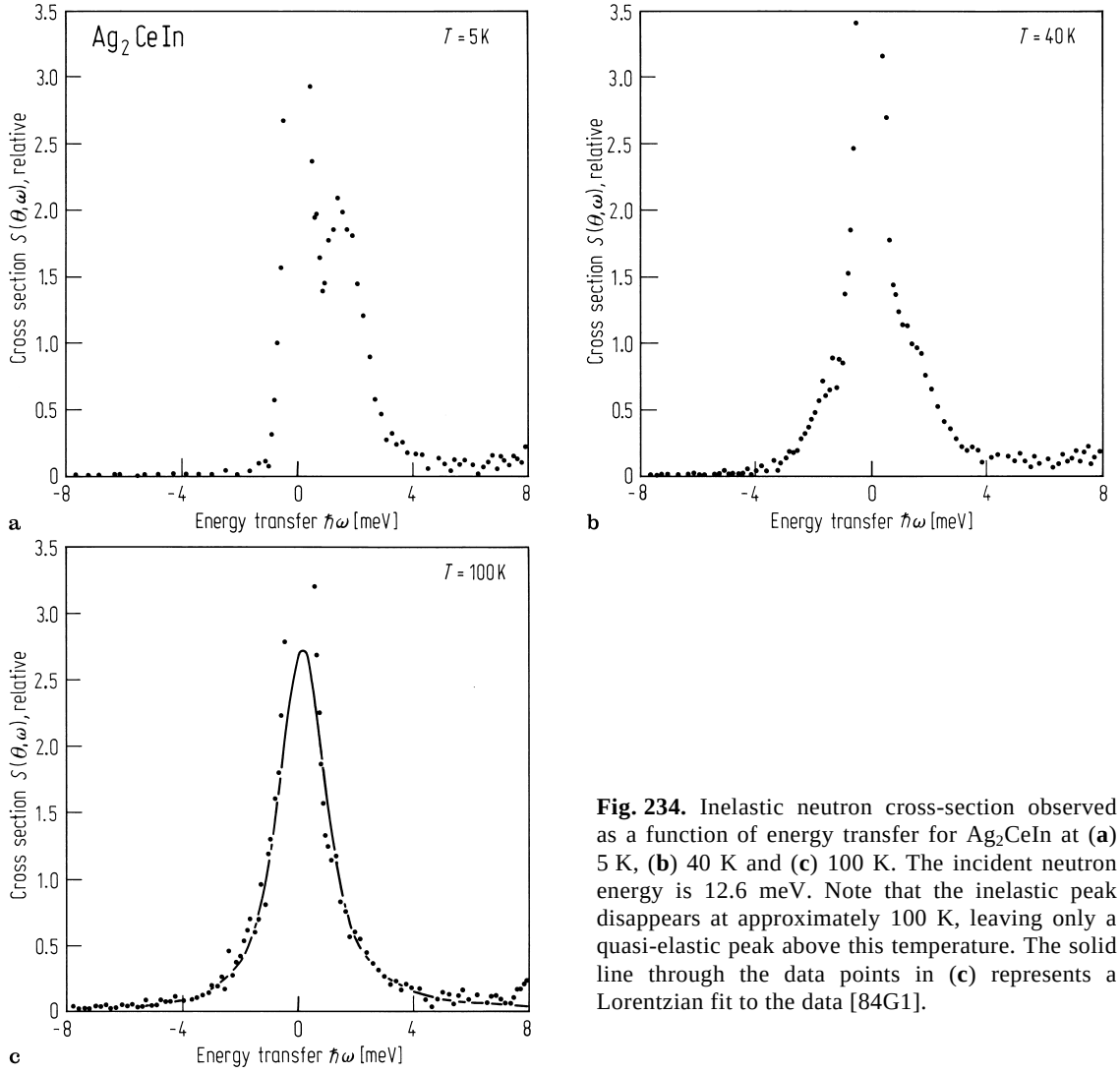

Fig. 234. Inelastic neutron cross-section observed as a function of energy transfer for Ag_2CeIn at (**a**) 5 K, (**b**) 40 K and (**c**) 100 K. The incident neutron energy is 12.6 meV. Note that the inelastic peak disappears at approximately 100 K, leaving only a quasi-elastic peak above this temperature. The solid line through the data points in (**c**) represents a Lorentzian fit to the data [84G1].

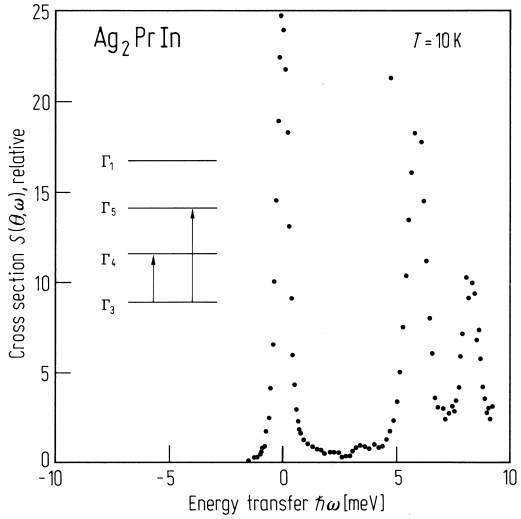

Fig. 235. Normalised neutron cross-section of Ag_2PrIn vs. energy transfer at 10 K. Two transitions at 5.9 and 8.3 meV are observed with a third at 2 meV becoming visible at 80 K. Since the ground state is non-magnetic it is assigned a Γ_3 doublet with the peaks at 5.9 meV corresponding to the $\Gamma_3 \leftrightarrow \Gamma_4$ and $\Gamma_3 \leftrightarrow \Gamma_5$ transitions, respectively [84G1].

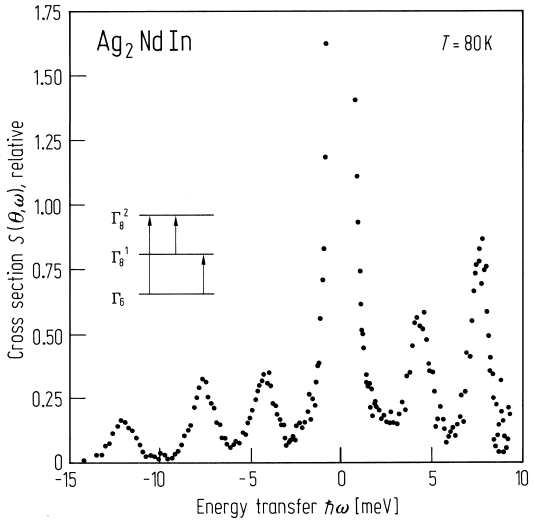

Fig. 236. Normalised neutron cross-section of Ag_2NdIn at 80 K. The level scheme and possible transitions are indicated in the figure [84G1].

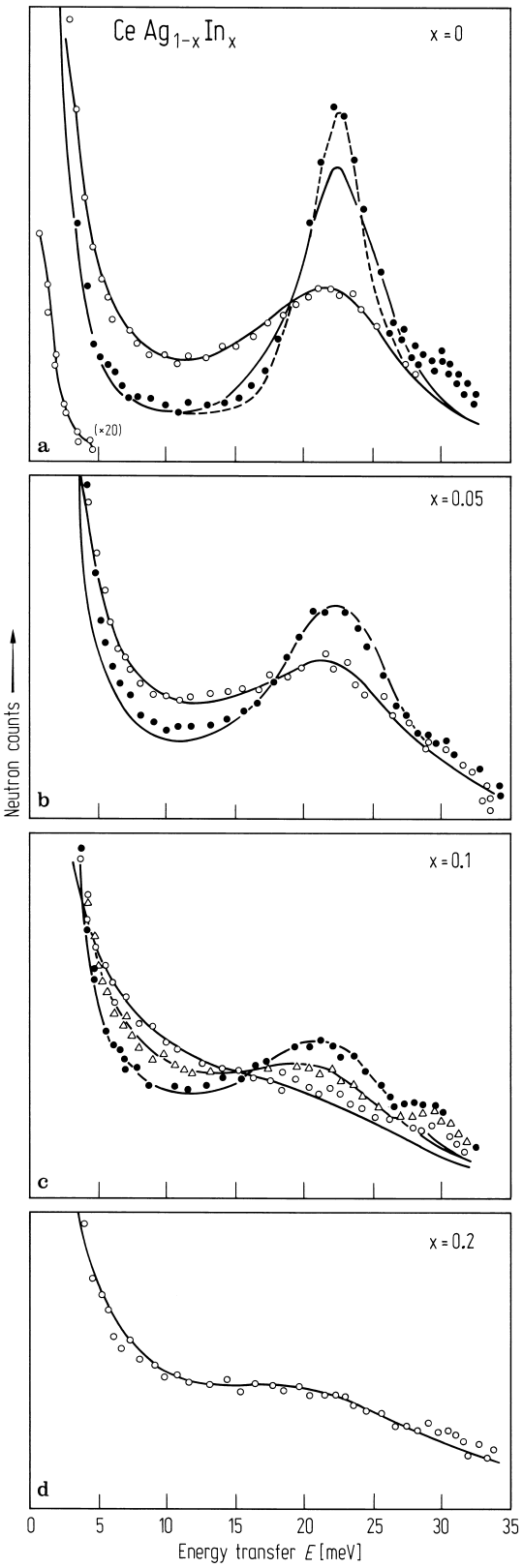

Fig. 237. The inelastic neutron spectra in the cubic phase of $CeAg_{1-x}In_x$ The full curves and the dashed curve are fits. (**a**) x = 0: T = 20 K (solid circles) and 140 K (open circles); (**b**) x = 0.05: T = 80 K (solid circles) and 150 K (open circles); (**c**) x = 0.1: T = 110 K (solid circles), 165 K (triangles) and 250 K (open circles); (**d**) x = 0.2: T = 150 K [82W1].

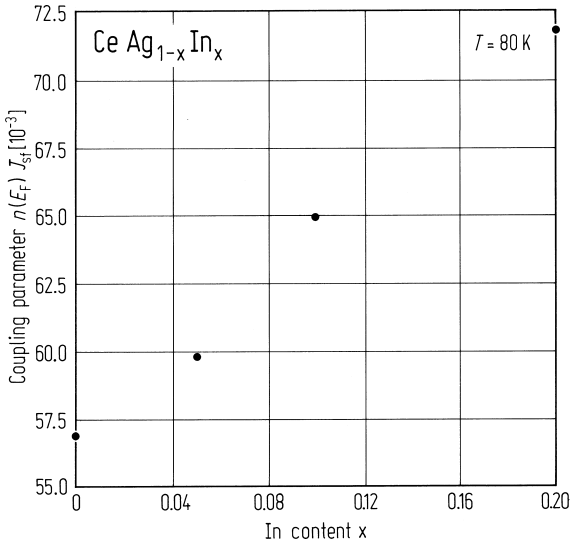

Fig. 238. The k-f coupling parameter $n(E_F)J_{sf}$ as a function of the In concentration x in $CeAg_{1-x}In_x$ [82W1].

1.5.5.5 Phase transitions

Several Heusler alloys, e.g. Ni_2MnGa, Co_2NbSn etc. undergo structural phase transitions at low temperatures. These transitions are believed to be driven by a band Jahn Teller mechanism. As yet there has not been any experimental evidence to confirm this conjecture. Heusler compounds have proved good model systems for studying the dynamics of atomic order. In general Heusler alloys pass from complete random disorder, the A2 structure, through B2 order, the CsCl structure, to the Heusler $L2_1$ arrangement. The A2-B2 ordering temperature is usually denoted by T_2 and the B2-$L2_1$ ordering temperature by T_1.

Heusler alloys in which the magnetic moment is confined to the Mn atom are good local moment systems. In these compounds the manganese moment, which is usually close to 4 μ_B, remains fixed in amplitude when going from the ordered to the paramagnetic state. For these Heusler alloys there is negligible overlap of the Mn d-electron wave functions and the d-band does not participate in the Fermi surface. However, the situation is potentially different for those systems in which the moment is associated with the X atoms or both the X and Y atoms. For such compounds the magnetic atoms are close enough for significant overlap of the d wave function to occur. Hence spin fluctuations may be important. However, thermal expansion measurements have failed to reveal any anomalies at the Curie temperature in Co_2MnZ compounds. This would suggest that the magnetic moments are of fixed amplitude. Similar results were also found in $Ni_{3-x}MnSn$.

Table 53. Melting points of some Heusler alloys [90M1].

Compounds	T_m [°C]
Cu_2MnAl	948
Co_2MnSn	1028
Ni_2MnSn	1125
Ni_2ZrSn	968
Ni_2ZrIn	864